ACSNANO

www.acsnano.org

ARTICLE

Continuous Wave Sum Frequency Generation and Imaging of Monolayer and Heterobilayer Two-Dimensional Semiconductors

Kaiyuan Yao, Emanuil Yanev, Hsun-Jen Chuang, Matthew R. Rosenberger, Xinyi Xu, Thomas Darlington, Kathleen M. McCreary, Aubrey T. Hanbicki, Kenji Watanabe, Takashi Taniguchi, Berend T. Jonker, Xiaoyang Zhu, D. N. Basov, James C. Hone, and P. James Schuck*

Cite This: https://dx.doi.org/10.1021/acsnano.9b07555

Read Online

ACCESS | Metrics & More | Article Recommendations | Supporting Information

ABSTRACT: We report continuous-wave second harmonic and sum frequency generation from two-dimensional transition metal dichalcogenide monolayers and their heterostructures with pump irradiances several orders of magnitude lower than those of conventional pulsed experiments. The high nonlinear efficiency originates from above-gap excitons in the band nesting regions, as revealed by wavelength-dependent second order optical susceptibilities quantified in four common monolayer transition metal dichalcogenides. Using sum frequency excitation spectroscopy and imaging, we identify and distinguish one- and two-photon resonances in both monolayers and heterobilayers. Data for heterostructures reveal responses from constituent layers accompanied by nonlinear signal correlated with interlayer transitions. We demonstrate spatial mapping of heterogeneous interlayer coupling by sum frequency and second harmonic confocal microscopy on heterobilayer $MoSe_2/WSe_2$.

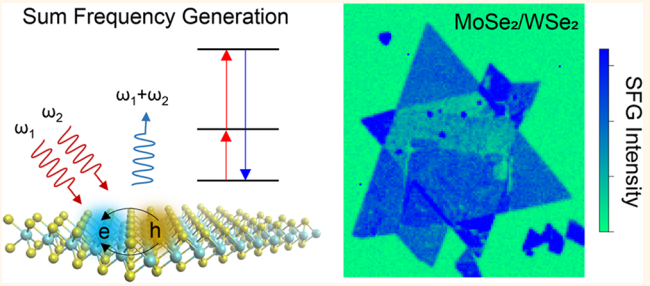

KEYWORDS: *nonlinear optics, sum frequency generation, exciton, two-dimensional semiconductors, van der Waals heterostructures, confocal microscopy, valleytronics*

Nonlinear optical spectroscopy and microscopy are proving crucial to the development and study of two-dimensional (2D) layered materials and emerging van der Waals (vdW) quantum materials.[1,2] Second order nonlinear processes such as second harmonic generation (SHG) originate from noncentrosymmetric crystal structure and have been widely used for the determination of layer number, crystal orientation, and twist angle of atomically thin transition metal dichalcogenides (TMDs), hexagonal boron nitrides (hBN), vdW heterostructures,[3−5] and Weyl semimetals.[6] Nonlinear microscopy can provide direct imaging of symmetry-related local information such as crystal domains,[7,8] strain fields,[9,10] edge disorders,[11] etc. Recently, SHG was also shown to be a powerful probe of the antiferromagnetic coupling in layered magnets.[12]

Conventionally, nonlinear optical characterization of 2D layered materials is performed with pulsed excitation lasers with high instantaneous pump irradiances of the order of tens to hundreds of TeraW/m^2.[2,3,7,13−15] The relatively high pump fluence can induce significant carrier-renormalization effects that substantially alter the intrinsic electronic band structure and screen exciton states.[16−19] In addition, multibeam nonlinear experiments such as sum frequency generation (SFG) and four-wave mixing[20] are ultrasensitive to the temporal overlap of multiple laser pulses at different wavelengths, thus posing stringent limits on the applicability, versatility, and robustness of complex and broadband nonlinear optical characterization methods.

In this work, we report the continuous wave (CW) generation of second order nonlinear signals from 2D TMDs and their heterostructures with pump irradiances that are more than 3 orders of magnitude lower than those of typical pulsed excitation conditions. Wavelength-dependent second order nonlinear optical susceptibilities are measured for monolayer (1L) MoS_2, WS_2, $MoSe_2$, WSe_2, and twisted heterobilayers of $MoSe_2/WSe_2$, providing a clear comparison of their efficiencies

Received: September 24, 2019
Accepted: December 31, 2019
Published: December 31, 2019

as a useful guideline for both material characterization and device applications. More importantly, based on robust CW operation, we report multimodal SFG excitation spectroscopy and microscopy, demonstrating their applications in the study of exciton resonances, interlayer electronic coupling, and valley contrasting physics. In particular, we show that nonlinear microscopy can be an effective and nondestructive method for spatial visualization of interlayer coupling in vdW heterostructures and quality inspection of heterobilayer samples.

RESULTS AND DISCUSSION

A representative confocal CW SHG image of a mechanically exfoliated WSe_2 flake is shown in Figure 1a under excitation by

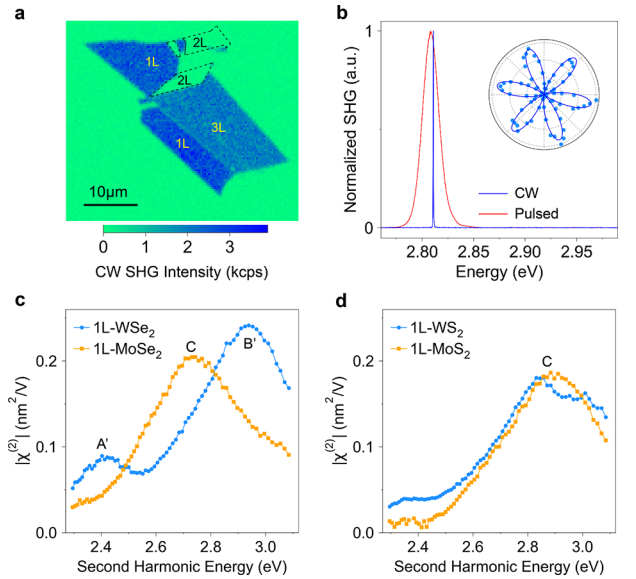

Figure 1. Observation of CW SHG from monolayer transition metal dichalcogenides. (a) Confocal microscopy of SHG intensity from exfoliated WSe_2 flakes (no hBN encapsulation) pumped by a CW laser at 1.406 eV with incident irradiance of 10^{10} W/m^2. kcps, kilocounts per second. (b) Comparison of SHG spectra under CW and pulsed excitation. Inset shows the polarization-dependent CW SHG intensity measured from the monolayer (1L) region in panel a. Wavelength-dependent characterization of second order sheet susceptibilities $|\chi^{(2)}|$ of (c) 1L-WSe_2 and 1L-$MoSe_2$ and (d) 1L-WS_2 and 1L-MoS_2, showing large enhancements due to resonances with A′, B′, and C excitons.

a 1.406 eV CW laser with irradiance of 10^{10} W/m^2. Strong CW SHG signals are observed in the monolayer and trilayer regions, which belong to the D_{3h} space group with broken inversion symmetry, and negligible signals are collected from the bilayer region with centrosymmetric crystal structure. The CW SHG count rates in Figure 1a are directly measured from the detector without applying any correction based on system collection efficiency. Figure 1b shows the normalized spectrum of CW SHG with a narrow, pump-limited line width, significantly narrower than the SHG excited by our 120 fs pulses. The inset of Figure 1b shows polarization-dependent CW SHG intensity measured with collinearly polarized pump and second harmonic signals, acquired from the monolayer region of the flake shown in Figure 1a. The 6-fold flower pattern follows from the second order susceptibility tensor: $|\chi^{(2)}| = \chi^{(2)}_{yyy} = -\chi^{(2)}_{yxx} = -\chi^{(2)}_{xxy} = -\chi^{(2)}_{xyx}$ with y being the armchair direction and x being the zigzag direction.[3] The layer dependence and polarization dependence of CW SHG signals confirm that the CW nonlinear signals are generated from the intrinsic TMD crystal lattice instead of defects or contamination.

The capability to observe SHG with low pump irradiance reveals the intrinsically high nonlinear efficiency in monolayer TMDs. SHG excitation spectroscopy was performed to quantify the wavelength-dependent second order sheet susceptibility $|\chi^{(2)}|$ for monolayer WSe_2, $MoSe_2$, WS_2, and MoS_2 (Figure 1c, d). All samples used for $|\chi^{(2)}|$ measurements are mechanically exfoliated and transferred onto fused silica substrates with thin (<20 nm) hBN encapsulation layers to avoid substrate-induced interference effects.[21] The quantitative values of $|\chi^{(2)}|$ are obtained by comparing SHG intensity measured on monolayers to reference samples of z-cut quartz crystals at each excitation wavelength.[3,22] With the same pump wavelengths and substrate, our data agree reasonably well with previous reports for 1L-MoS_2.[3,14] For all four monolayer TMDs, $|\chi^{(2)}|$ is greatly enhanced when the second harmonic energy becomes resonant with their respective high-energy exciton states above the optical gap, which are labeled as A′ and B′ excitons for 1L-WSe_2 and C excitons for 1L-$MoSe_2$, 1L-WS_2, and 1L-MoS_2.[23,24] When on resonance with these excitons, $|\chi^{(2)}|$ values of the four 1L-TMDs are all found to be approximately 0.2 nm^2/V, which are much higher than previous reports[25−27] at other second harmonic energies.

Despite the clear observation of peaks in the $|\chi^{(2)}|$ spectra, SHG excitation spectroscopy cannot fully distinguish between one- and two-photon resonances. Here, a one-photon resonance refers to the energetic resonance of the pump photon, and a two-photon resonance refers to energetic resonance of the second harmonic or sum frequency photon. Second order nonlinear transitions are doubly resonant processes, as sketched by the level diagram in Figure 2a.[22,28,29] The underlying resonances can be discriminated unambiguously by SFG excitation spectroscopy, where energies of the two pump photons can be separately controlled. Figure 2b shows a representative CW SFG spectrum from 1L-WSe_2 pumped by two spatially overlapped CW laser beams at ω_1 (1.27 eV) and ω_2 (1.406 eV). Three pronounced peaks at $2\omega_1$, $\omega_1+\omega_2$, and $2\omega_2$ can be observed at the same time. The inset of Figure 2b shows the dependence of intensities of the three signals on pump irradiance of ω_2, showing linear power dependence for the SFG signal and quadratic power dependence for the $2\omega_2$ SHG signal, confirming our peak assignments.

In our SFG excitation spectroscopy, one pump frequency is fixed at ω_1, and the second pump frequency ω_2 is continuously tuned, generating SFG and SHG signals together at different frequencies. Figure 2c shows the heat map of nonlinear signal intensity as a function of pump excitation energy and output photon energy for 1L-WSe_2. The SFG intensity at $\omega_1 + \omega_2$ and SHG intensity at $2\omega_2$ are extracted and plotted as a function of their respective output photon energy in Figure 2d. Interestingly, both SFG and SHG are significantly enhanced when their nonlinear output energies approach A′ and B′ excitons at 2.4 and 2.9 eV, respectively, regardless of how the output energy is distributed between the two contributing pump photons. The SHG and SFG excitation spectra are also identical except for the rapid drop of SFG above 2.87 eV, which is discussed later. This provides evidence that the final transition from excited state $|e\rangle$ to ground state $|g\rangle$ is the dominant resonance in the level diagram shown by Figure 2a.

https://dx.doi.org/10.1021/acsnano.9b07555
ACS Nano XXXX, XXX, XXX−XXX

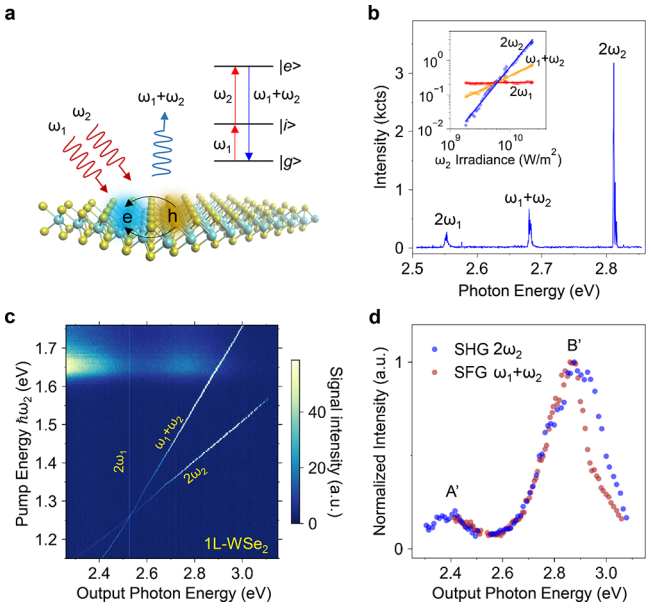

Figure 2. SFG excitation spectroscopy of 1L-WSe_2. (a) Schematics of exciton-resonance-enhanced SFG process where two pump photons with energies of $\hbar\omega_1$ and $\hbar\omega_2$ are upconverted into one photon with a summed energy of $\hbar\omega_1 + \hbar\omega_2$. Inset: level diagram of the SFG process. (b) Typical spectrum of CW SFG. Inset: the dependence of SFG and SHG intensities on the irradiance of the pump beam at ω_2. Solid lines are power law fits with power coefficients of 0.03, 0.92, and 1.96 for $2\omega_1$, $\omega_1 + \omega_2$, and $2\omega_2$, respectively. (c) Heat map of SFG CW excitation spectroscopy. In addition to the straight lines representing SHG and SFG signals, hot photoluminescence is also observed in odd layer WSe_2 (Figure S2), which may be excited by high energy SHG/SFG photons. (d) Dependence of SHG ($2\omega_2$) and SFG ($\omega_1 + \omega_2$) intensities on the output photon energy.

Similar results are obtained on other monolayer TMDs and are included in the Supporting Information.

The output-dominated resonance behavior likely arises from the high oscillator strengths of A′ and B′ excitons in 1L-WSe_2. Similarly, enhanced SHG/SFG signals are observed when output photon energies approach the C excitons for 1L-MoS_2, 1L-$MoSe_2$, and 1L-WS_2 (Supporting Information, Figure S1). In monolayer TMDs, band nesting effects result in a large joint density of states (JDOS) as conduction and valence bands become parallel.[24] Therefore, the resonant enhancement of nonlinear efficiency may be explained by the enhanced transition rate from the two-photon excited state $|e\rangle$ to the ground state $|g\rangle$ due to the large JDOS.

In fact, our data also show that directly pumping excitonic resonances is highly undesirable for nonlinear optical applications due to strong photocarrier renormalization effects. As mentioned before, the SFG intensity becomes strongly suppressed compared to SHG when the sum frequency photon energy goes above 2.9 eV. In this regime, the excitation energy $\hbar\omega_2$ exceeds the optical gap at 1.65 eV, resulting in the generation of a large concentration of excess carriers, which is estimated to be about 5×10^{13} cm^{-2}, considering a pump irradiance of 10^{10} W/m^2, optical absorption of 5%,[23] and photocarrier relaxation time of 300 ps.[30] The high density of excess photocarriers may induce strong Coulomb screening[31] of the band nesting excitons, resulting in lower exciton oscillator strength and consequently reduced nonlinear efficiency. This is further evidenced by measurements of SFG efficiency as a function of pump irradiance, comparing pump energies below and above the optical absorption gap (Figure S8). In addition to the photocarrier effects, depletion of the pump by direct linear absorption may also play a role in reducing nonlinear efficiency. Disentangling the convoluted pump and output energetic resonances and renormalization effects in 2D semiconductors can provide critical guidelines for designing excitonic nonlinear optical devices.

Next, we apply SFG microscopy and excitation spectroscopy to investigate interlayer coupling in vdW heterobilayers of $MoSe_2/WSe_2$. The TMD monolayers used here are grown by chemical vapor deposition and subsequently stacked together.[33] Figure 3a–c shows the nonlinear confocal images of a 58 ± 0.5° twisted heterobilayer sample. The twist angles are verified by polarization-dependent SHG measurements of the separate monolayer regions, as shown in the Supporting Information. The nonlinear signal at 2.75 eV corresponds to the sum frequency of the two laser beams, and the signals at 2.96 and 2.54 eV are SHG signals. Our as-stacked heterobilayer samples typically have tiny bubbles and wrinkles with <10 nm heights. The "nano-squeegee" method[32] is applied to create a flattened heterobilayer region, as shown by the box in Figure 3a. The flattening process is illustrated in Figure 3d, where an atomic force microscope (AFM) tip is scanned across the sample in contact mode to flatten and/or move bubbles and to sweep away contaminants on and within the heterobilayer.[34] This results in more intimate contact between the top and bottom monolayers of $MoSe_2$ and WSe_2, as evidenced by AFM topography images shown in the Supporting Information. The nano-squeegee method has been shown to be effective in enhancing interlayer electronic coupling.[32,33] Here, we observe significantly enhanced nonlinear efficiency in the flattened heterobilayer region compared to the as-stacked heterobilayer region (Figure 3a–c).

For heterobilayer TMDs with a twist angle close to 60°, it has been reported that the SHG intensity would be strongly quenched compared to bare monolayers, which was explained by destructive optical interference of the second harmonic waves generated from electrically decoupled top and bottom layers.[4] In our microscopy images, SHG and SFG are consistently quenched in the as-stacked heterobilayer region but enhanced to brightnesses comparable to monolayers in the flattened region despite having a twist angle close to 60°. The flattening-induced enhancement of SFG is stronger than that of SHG because the sum frequency photon energy is closer to the interlayer resonance. The enhanced nonlinearity is further evidenced by the $|\chi^{(2)}|$ spectra measured in the flattened region versus the as-stacked region (Figure 3e), showing that the heterobilayer $|\chi^{(2)}|$ peak at about 2.85 eV is stronger in the flattened region. Because the flattening process has been known to enhance interlayer electronic coupling,[33] we tentatively attribute this feature to be an interlayer electronic transition that resonantly enhances SHG and SFG. The flattening-induced nonlinear enhancement is also observed in a second 0° twisted heterobilayer sample (Figure S6). The clear correlation between nonlinear generation intensity and interlayer coupling suggests that interlayer electronic transitions can play an important role in SHG and SFG from twisted heterobilayers.

The $|\chi^{(2)}|$ of our 58° $MoSe_2/WSe_2$ is largest when the pump energy $\hbar\omega_2$ is around 1.4 eV (second harmonic energy $2\omega_2$ around 2.8 eV), which is close to the energy of interlayer excitons in this heterobilayer system.[33,35,36] SFG excitation

https://dx.doi.org/10.1021/acsnano.9b07555
ACS Nano XXXX, XXX, XXX−XXX

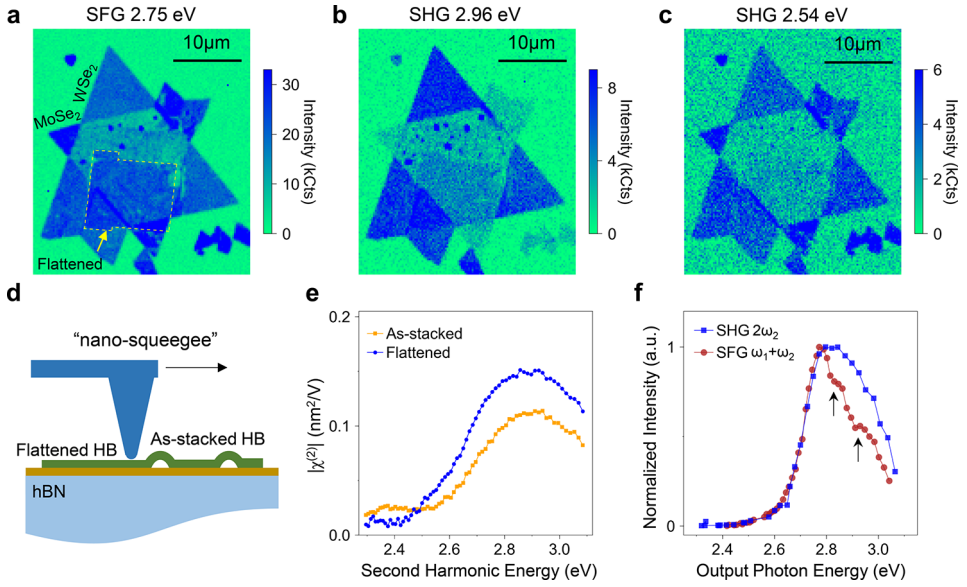

Figure 3. Revealing interlayer coupling in vdW heterostructures by nonlinear confocal microscopy and excitation spectroscopy. Microscopy images of SFG (a) and SHG (b, c) on a 58° twisted heterobilayer (HB) of $MoSe_2/WSe_2$ with spatially overlapped dual-beam CW laser excitation at 1.27 and 1.476 eV. The dashed box in panel a indicates the region flattened by the nano-squeegee process[32] as illustrated in panel d, where an AFM tip is scanned in contact mode to flatten out bubbles and wrinkles. Note that in panel d, the substrate and top hBN layer are omitted for clarity, and the sketch is not in scale. (e) Spectra of second order nonlinear susceptibility $|\chi^{(2)}|$ showing enhanced nonlinear efficiency in the flattened region at corresponding output photon energies consistent with confocal microscopy. (f) SFG excitation spectroscopy with ω_2 being scanned and ω_1 fixed at 1.27 eV. The arrows indicate carrier renormalization effects when ω_2 matches the A exciton energy of 1L-$MoSe_2$ and 1L-WSe_2.

spectroscopy is performed to distinguish one-photon (pump) and two-photon (output) resonances. Similar to Figure 2, one pump frequency ω_1 is kept constant (1.27 eV), while the second pump ω_2 is continuously scanned. If the $|\chi^{(2)}|$ peak in Figure 3e was related to the pump resonance of a band edge interlayer exciton at 1.4 eV, SHG and SFG would be enhanced when pump energy $\hbar\omega_2$ reaches 1.4 eV, leading to maximized second harmonic and sum frequency generation at 2.8 and 2.67 eV, respectively. Instead, the excitation spectra of SFG and SHG are almost identical for their dependence on output energy. Therefore, we tentatively assign the peak in the $|\chi^{(2)}|$ spectrum to be an output-resonant higher energy interlayer transition, possibly with excitonic nature.

Furthermore, carrier-induced Coulomb screening and renormalization effects[16,17] are also found to strongly affect nonlinear processes in heterobilayers. In Figure 3f, the two arrows indicate the position when the pump photon energy $\hbar\omega_2$ is scanned to be resonant with A excitons of the 1L-$MoSe_2$ and the 1L-WSe_2 in the heterobilayer. Similar to the monolayer TMDs, rapid drops in nonlinear efficiency are observed when pump energies are directly resonant with excitons.

Finally, we examine the linear polarization dependence and chirality selection rules of SFG in monolayer TMDs. In our linear polarization experiments, the electric field of ω_1 is fixed along the armchair direction while the beam at ω_2 is rotated, as sketched by Figure 4a. We found that the total SFG intensity does not depend on the cross-polarization angle $\Delta\theta$ of the two pump beams, as shown by the nonpolarized SFG intensity in Figure 4b. However, the linearly polarized components of the sum frequency electric field along the armchair and zigzag directions are indeed dependent on $\Delta\theta$. It can be derived from the $\chi^{(2)}$ tensor that

$$I_y^{\omega_1+\omega_2} = |\chi^{(2)}|^2 I^{\omega_1} I^{\omega_2} \cos^2(\Delta\theta) \quad (1)$$

$$I_x^{\omega_1+\omega_2} = |\chi^{(2)}|^2 I^{\omega_1} I^{\omega_2} \sin^2(\Delta\theta) \quad (2)$$

where $I_y^{\omega_1+\omega_2}$ and $I_x^{\omega_1+\omega_2}$ represents the SFG intensity along armchair and zigzag directions, respectively, and I^{ω_1} and I^{ω_2} are intensities of the two pump beams. The solid lines in Figure 4b are fitting results of the experimental data using eqs 1 and 2.

Perhaps more interestingly for these candidate valleytronics materials, the circular polarization dependence of SFG is also investigated. In our experiments, 1.27 and 1.148 eV CW laser beams are used for excitation with separate control of their circular polarization states. No analyzers are placed in the collection path. In Figure 4c, the right (left) circularly polarized pump beam is denoted by $\sigma+(-)$. The $2\omega_2$ and $\omega_1 + \omega_2$ peaks are much stronger because they are close to the B exciton resonance of 1L-WS_2 at 2.4 eV. Strong SFG can only be observed when the two pump beams have the same circular polarization and almost vanishes when the two pumps have opposite chirality. This chirality selection rule of SFG originates from threefold rotational symmetry of the crystal lattice of monolayer TMDs.[37] For generic second order nonlinear processes, it can be shown that

$$\sigma_{\omega_1} + \sigma_{\omega_2} - \sigma_{\omega_1+\omega_2} = 3N,\ N = 0,\ 1,\ 2\ldots \quad (3)$$

where σ_{ω_1}, σ_{ω_2}, and $\sigma_{\omega_1+\omega_2}$ are the circular polarizations of the two pump photons and the generated sum frequency photon. More detailed discussions are included in the Supporting Information. The K and −K valleys of monolayer TMDs are selectively coupled to different circular polarizations of light as a result of inversion symmetry breaking and spin−orbit coupling.[38,39] When two pump photons have identical chirality, SFG follows the same valley-coupled chirality selection rule as previously reported for SHG.[26,37,40] When two pump photons have opposite chirality, SFG is found to be a forbidden process, as sketched in Figure 4d, consistent with the theoretical result

https://dx.doi.org/10.1021/acsnano.9b07555
ACS Nano XXXX, XXX, XXX−XXX

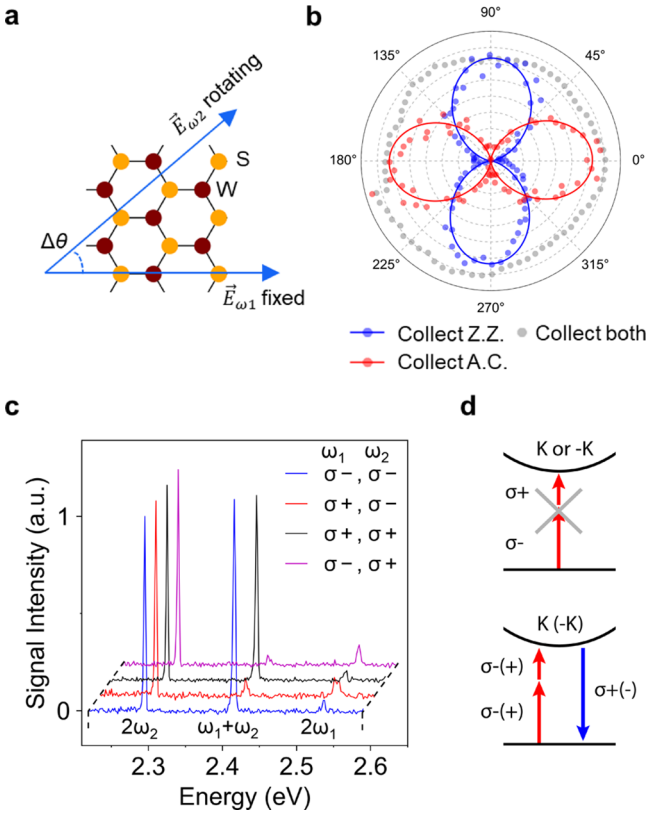

Figure 4. Polarization dependence and chirality selection rules of sum frequency generation from monolayer WS_2. (a) Illustration of the pump polarization $\vec{E}_{\omega_1}$ and $\vec{E}_{\omega_2}$ with respect to the lattice of monolayer WS_2. (b) Dependence of polarized SFG intensities on the cross-polarization angle $\Delta\theta$ between two pump beams. Blue and red show the SFG components polarized along zigzag (ZZ) and armchair (AC) directions, respectively. The total SFG intensity is *not* affected by the collinearity of the two pump beams. (c) SFG and SHG spectra excited by two pump beams of different combinations of circular-polarization states, with σ+(−) representing right (left) circularly polarized light. (d) Illustration of the valley-coupled chirality selection rule showing forbidden SFG from two pump photons with opposite chirality (upper) and the σ+(−) polarized SFG scattered from K(−K) valleys (lower).

of eq 3. This SFG chirality selection rule may inspire optical methods for the study of valley physics.

CONCLUSION

In conclusion, continuous-wave generation of second harmonic and sum frequency signals is realized from atomically thin transition metal dichalcogenides and van der Waals heterostructures. Nonlinear optical spectroscopy and microscopy techniques are developed based on CW operation for probing optical and electronic properties. In particular, we demonstrate the application of SFG excitation spectroscopy in discriminating one-photon (pump) versus two-photon (output) excitonic resonances in nonlinear processes and SFG/SHG microscopy for spatial imaging of interlayer coupling in twisted heterobilayers of $MoSe_2/WSe_2$. In addition, the linear and circular polarization dependence of SFG is fully investigated. Our results provide insights on nonlinear optics in van der Waals quantum materials as well as guidelines for next-generation nonlinear optical devices based on 2D semiconductors.

METHODS

Measurement of Nonlinear Susceptibility. A wavelength-tunable Ti:sapphire laser (Coherent Chameleon) is used as a pulsed pump source with pulse duration of about 120 fs. A feedback control system made of a continuously motorized neutral density filter wheel and power meter is used to regulate the pump power. The pump beam is focused onto the sample using a 100×, 0.95 numerical aperture objective. SHG signals are collected in a backscattering geometry, dispersed by a spectrometer, and measured by a cooled silicon CCD camera. Wavelength-dependent SHG intensities of monolayer and heterobilayer TMD samples are measured and compared to the reference sample of a 1 mm-thick z-cut quartz crystal. The following formula[3] is used to obtain nonlinear susceptibility $|\chi^{(2)}|$ from the measured SHG intensity from monolayer and heterobilayer samples (I_S) and from the reference crystal (I_{quartz}). In the following, $|\chi_S^{(2)}|$ is the sheet susceptibility, d_s is the thickness of respective monolayer or bilayer samples, $|\chi^{(2)}_{quartz,11}|$ is the susceptibility value of z-cut quartz along its 11 direction and taken to be 0.3 pm/V and constant across the wavelength range of our measurements,[41] I_S and I_{quartz} are SHG intensities measured on the sample and on z-cut quartz, both normalized to the square of pump power, $n(\omega)$ and $n(2\omega)$ are the refractive indexes of the fused silica substrate at pump and second harmonic wavelengths, respectively, and c is speed of light in a vacuum.

$$\frac{|\chi_S^{(2)}|/d_s}{|\chi^{(2)}_{quartz,11}|} = \frac{c}{4\omega[n(\omega)+n(2\omega)]}\sqrt{\frac{I_S}{I_{quartz}}}$$

Continuous Wave SFG Microscopy and Excitation Spectroscopy. For CW experiments, the aforementioned Ti:sapphire laser is operated without mode-locking as the tunable pump beam, and a 1.27 eV diode laser is used as the second pump beam with fixed wavelength. The backscattered SFG and SHG spectra are collected with a thermoelectrically cooled electron multiplying CCD (EMCCD) (Princeton Instrument ProEM). Typical integration time is 0.3 s for excitation spectroscopy and 0.1s for microscopy. The typical pump beam spot size is about 600 nm, and typical CW pump power is in the range of 1−20 mW. All experiments are performed at room temperature and in ambient conditions. No visible sample damage has been observed under CW excitation.

Sample Preparation. Flakes of TMDs are mechanically exfoliated onto 285 or 90 nm SiO_2/Si substrates and then transferred onto fused silica substrates for wavelength-dependent nonlinear measurements. Heterobilayer samples are prepared following methods reported before.[32,33] MoS_2 and WS_2 bulk crystals are purchased from HQ Graphene. $MoSe_2$ and WSe_2 bulk crystals are home grown by the flux method.[42] The hBN bulk crystals are provided by National Institute for Materials Science, Tsukuba, Japan. Standard mechanical exfoliation is performed with Scotch tape to obtain mono- and few-layer TMD and hBN flakes. The mother tapes for TMD are heated at 100 C° and then sufficiently cooled prior to exfoliation. Layer transfer and hBN encapsulation follows standard dry-transfer techniques with a polypropylene carbonate film on a polydimethylsiloxane stamp.[43]

ASSOCIATED CONTENT

Supporting Information

The Supporting Information is available free of charge at https://pubs.acs.org/doi/10.1021/acsnano.9b07555.

SFG and SHG measurements on additional samples, photoluminescence and AFM data from heterobilayers, and supplementary discussions (PDF)

AUTHOR INFORMATION

Corresponding Author

P. James Schuck − *Columbia University, New York, New York;* orcid.org/0000-0001-9244-2671;
Email: p.j.schuck@columbia.edu

https://dx.doi.org/10.1021/acsnano.9b07555
ACS Nano XXXX, XXX, XXX−XXX

Other Authors

Kaiyuan Yao − *Columbia University, New York, New York, and University of California, Berkeley, Berkeley, California*

Emanuil Yanev − *Columbia University, New York, New York*

Hsun-Jen Chuang − *Naval Research Laboratory, Washington, D.C.*

Matthew R. Rosenberger − *Naval Research Laboratory, Washington, D.C.;* orcid.org/0000-0001-6866-5488

Xinyi Xu − *Columbia University, New York, New York*

Thomas Darlington − *Columbia University, New York, New York, and University of California, Berkeley, Berkeley, California*

Kathleen M. McCreary − *Naval Research Laboratory, Washington, D.C.;* orcid.org/0000-0003-2737-585X

Aubrey T. Hanbicki − *Naval Research Laboratory, Washington, D.C., and Laboratory for Physical Sciences, College Park, Maryland*

Kenji Watanabe − *National Institute for Materials Science, Tsukuba, Japan*

Takashi Taniguchi − *National Institute for Materials Science, Tsukuba, Japan*

Berend T. Jonker − *Naval Research Laboratory, Washington, D.C.*

Xiaoyang Zhu − *Columbia University, New York, New York;* orcid.org/0000-0002-2090-8484

D. N. Basov − *Columbia University, New York, New York*

James C. Hone − *Columbia University, New York, New York*

Complete contact information is available at: https://pubs.acs.org/10.1021/acsnano.9b07555

Notes

The authors declare no competing financial interest.

ACKNOWLEDGMENTS

This work is supported as part of Programmable Quantum Materials, an Energy Frontier Research Center funded by the U.S. Department of Energy (DOE), Office of Science, Basic Energy Sciences (BES), under Award DE-SC0019443. The work at NRL was supported by core research programs within the Materials/Chemistry and Nanoscience Focus Areas. H.J.C. and M.R.R. gratefully acknowledge support through the ASEE and NRC postdoctoral associate programs at NRL, respectively.

REFERENCES

(1) Basov, D. N.; Averitt, R. D.; Hsieh, D. Towards Properties on Demand in Quantum Materials. *Nat. Mater.* **2017**, *16*, 1077−1088.

(2) Autere, A.; Jussila, H.; Dai, Y.; Wang, Y.; Lipsanen, H.; Sun, Z. Nonlinear Optics with 2D Layered Materials. *Adv. Mater.* **2018**, *30*, 1705963.

(3) Li, Y.; Rao, Y.; Mak, K. F.; You, Y.; Wang, S.; Dean, C. R.; Heinz, T. F. Probing Symmetry Properties of Few-Layer MoS2 and h-BN by Optical Second-Harmonic Generation. *Nano Lett.* **2013**, *13*, 3329−3333.

(4) Hsu, W. T.; Zhao, Z. A.; Li, L. J.; Chen, C. H.; Chiu, M. H.; Chang, P. S.; Chou, Y. C.; Chang, W. H. Second Harmonic Generation from Artificially Stacked Transition Metal Dichalcogenide Twisted Bilayers. *ACS Nano* **2014**, *8*, 2951−2958.

(5) Jin, C.; Regan, E. C.; Yan, A.; Utama, M. I. B.; Wang, D.; Zhao, S.; Qin, Y.; Yang, S.; Zheng, Z.; Shi, S.; Watanabe, K.; Taniguchi, T.; Tongay, S.; Zettl, A.; Wang, F. Observation of Moiré Excitons in WSe2/WS2 Heterostructure Superlattices. *Nature* **2019**, *567*, 76−80.

(6) Wu, L.; Patankar, S.; Morimoto, T.; Nair, N. L.; Thewalt, E.; Little, A.; Analytis, J. G.; Moore, J. E.; Orenstein, J. Giant Anisotropic Nonlinear Optical Response in Transition Metal Monopnictide Weyl Semimetals. *Nat. Phys.* **2017**, *13*, 350.

(7) Kumar, N.; Najmaei, S.; Cui, Q.; Ceballos, F.; Ajayan, P. M.; Lou, J.; Zhao, H. Second Harmonic Microscopy of Monolayer MoS2. *Phys. Rev. B: Condens. Matter Mater. Phys.* **2013**, *16*, 161403.

(8) Karvonen, L.; Säynätjoki, A.; Huttunen, M. J.; Autere, A.; Amirsolaimani, B.; Li, S.; Norwood, R. A.; Peyghambarian, N.; Lipsanen, H.; Eda, G.; Kieu, K.; Sun, Zhipei Rapid Visualization of Grain Boundaries in Monolayer MoS_2 by Multiphoton Microscopy. *Nat. Commun.* **2017**, *8*, 15714.

(9) Liang, J.; Zhang, J.; Li, Z.; Hong, H.; Wang, J.; Zhang, Z.; Zhou, X.; Qiao, R.; Xu, J.; Gao, P.; Liu, Z. Monitoring Local Strain Vector in Atomic-Layered MoSe2 by Second-Harmonic Generation. *Nano Lett.* **2017**, *17*, 7539−7543.

(10) Mennel, L.; Furchi, M. M.; Wachter, S.; Paur, M.; Polyushkin, D. K.; Mueller, T. Optical Imaging of Strain in Two-Dimensional Crystals. *Nat. Commun.* **2018**, *9*, 516.

(11) Yin, X.; Ye, Z.; Chenet, D. A.; Ye, Y.; O'Brien, K.; Hone, J. C.; Zhang, X. Edge Nonlinear Optics on a MoS_2 Atomic Monolayer. *Science* **2014**, *344*, 488−490.

(12) Sun, Z.; Yi, Y.; Song, T.; Clark, G.; Huang, B.; Shan, Y.; Wu, S.; Huang, D.; Gao, C.; Chen, Z.; McGuire, M.; Cao, T.; Xiao, D.; Liu, W.-T.; Yao, W.; Xu, X.; Wu, S. Giant Nonreciprocal Second-Garmonic Generation from Antiferromagnetic Bilayer CrI3. *Nature* **2019**, *572*, 497−501.

(13) Janisch, C.; Wang, Y.; Ma, D.; Mehta, N.; Elías, A. L.; Perea-López, N.; Terrones, M.; Crespi, V.; Liu, Z. Extraordinary Second Harmonic Generation in Tungsten Disulfide Monolayers. *Sci. Rep.* **2015**, *4*, 5530.

(14) Malard, L. M.; Alencar, T. V.; Barboza, A. P. M.; Mak, K. F.; De Paula, A. M. Observation of Intense Second Harmonic Generation from MoS_2 Atomic Crystals. *Phys. Rev. B: Condens. Matter Mater. Phys.* **2013**, *87*, 201401.

(15) Liu, H.; Li, Y.; You, Y. S.; Ghimire, S.; Heinz, T. F.; Reis, D. A. High-Harmonic Generation from an Atomically Thin Semiconductor. *Nat. Phys.* **2017**, *13*, 262.

(16) Yao, K.; Yan, A.; Kahn, S.; Suslu, A.; Liang, Y.; Barnard, E.; Tongay, S.; Zettl, A.; Borys, N. J.; Schuck, P. J. Optically Discriminating Carrier-Induced Quasiparticle Band Gap and Exciton Energy Renormalization in Monolayer MoS_2. *Phys. Rev. Lett.* **2017**, *119*, 087401.

(17) Liu, F.; Ziffer, M. E.; Hansen, K. R.; Wang, J.; Zhu, X. Direct Determination of Band-Gap Renormalization in the Photoexcited Monolayer MoS_2. *Phys. Rev. Lett.* **2019**, *122*, 246803.

(18) Pogna, E. A.; Marsili, M.; De Fazio, D.; Dal Conte, S.; Manzoni, C.; Sangalli, D.; Yoon, D.; Lombardo, A.; Ferrari, A. C.; Marini, A.; Cerullo, G. Photo-Induced Bandgap Renormalization Governs the Ultrafast Response of Single-Layer MoS_2. *ACS Nano* **2016**, *10*, 1182−1188.

(19) Wang, J.; Ardelean, J.; Bai, Y.; Steinhoff, A.; Florian, M.; Jahnke, F.; Xu, X.; Kira, M.; Hone, J.; Zhu, X. Y. Optical Generation of High Carrier Densities in 2D Semiconductor Heterobilayers. *Sci. Adv.* **2019**, *5*, No. eaax0145.

(20) Li, D.; Xiong, W.; Jiang, L.; Xiao, Z.; Rabiee Golgir, H.; Wang, M.; Huang, X.; Zhou, Y.; Lin, Z.; Song, J.; Ducharme, S.; Jiang, L.; Silvain, J.-F.; Lu, Y. Multimodal Monlinear Optical Imaging of MoS_2 and MoS_2-Based van der Waals Heterostructures. *ACS Nano* **2016**, *10*, 3766−3775.

(21) Merano, M. Nonlinear Optical Response of a Two-Dimensional Atomic Crystal. *Opt. Lett.* **2016**, *41*, 187−190.

(22) Raschke, M. B.; Hayashi, M.; Lin, S. H.; Shen, Y. R. Doubly-Resonant Sum-Frequency Generation Spectroscopy for Surface Studies. *Chem. Phys. Lett.* **2002**, *359*, 367−472.

(23) Zhao, W.; Ghorannevis, Z.; Chu, L.; Toh, M.; Kloc, C.; Tan, P. H.; Eda, G. Evolution of Electronic Structure in Atomically Thin Sheets of WS_2 and WSe_2. *ACS Nano* **2013**, *7*, 791−797.
(24) Kozawa, D.; Kumar, R.; Carvalho, A.; Amara, K. K.; Zhao, W.; Wang, S.; Toh, M.; Ribeiro, R. M.; Neto, A. C.; Matsuda, K.; Eda, G. Photocarrier Relaxation Pathway in Two-Dimensional Semiconducting Transition Metal Dichalcogenides. *Nat. Commun.* **2014**, *5*, 4543.
(25) Autere, A.; Jussila, H.; Marini, A.; Saavedra, J. R. M.; Dai, Y.; Säynätjoki, A.; Karvonen, L.; Yang, H.; Amirsolaimani, B.; Norwood, R. A.; Peyghambarian, N.; Lipsanen, H.; Kieu, K.; Javier García de Abajo, F.; Sun, Z. Optical Harmonic Generation in Monolayer Group-VI Transition Metal Dichalcogenides. *Phys. Rev. B: Condens. Matter Mater. Phys.* **2018**, *98*, 115426.
(26) Seyler, K. L.; Schaibley, J. R.; Gong, P.; Rivera, P.; Jones, A. M.; Wu, S.; Yan, J.; Mandrus, D. G.; Yao, W.; Xu, X. Electrical Control of Second-Garmonic Generation in a WSe_2 Monolayer Transistor. *Nat. Nanotechnol.* **2015**, *10*, 407−411.
(27) Le, C. T.; Clark, D. J.; Ullah, F.; Senthilkumar, V.; Jang, J. I.; Sim, Y.; Seong, M. J.; Chung, K. H.; Park, H.; Kim, Y. S. Nonlinear Optical Characteristics of Monolayer $MoSe_2$. *Ann. Phys.* **2016**, *528*, 551−559.
(28) Shen, Y. *The Principles of Nonlinear Optics*, Wiley-Interscience: New York, 1984.
(29) Wang, G.; Marie, X.; Gerber, I.; Amand, T.; Lagarde, D.; Bouet, L.; Vidal, M.; Balocchi, A.; Urbaszek, B. Giant Enhancement of the Optical Second-Harmonic Emission of WSe_2 Monolayers by Laser Excitation at Exciton Resonances. *Phys. Rev. Lett.* **2015**, *114*, 097403.
(30) Zhang, X. X.; You, Y.; Zhao, S. Y. F.; Heinz, T. F. Experimental Evidence for Dark Excitons in Monolayer WSe_2. *Phys. Rev. Lett.* **2015**, *115*, 257403.
(31) Chernikov, A.; Ruppert, C.; Hill, H. M.; Rigosi, A. F.; Heinz, T. F. Population Inversion and Giant Bandgap Renormalization in Atomically Thin WS_2 Layers. *Nat. Photonics* **2015**, *9*, 466−470.
(32) Rosenberger, M. R.; Chuang, H. J.; McCreary, K. M.; Hanbicki, A. T.; Sivaram, S. V.; Jonker, B. T. Nano-"Squeegee" for the Creation of Clean 2D Material Interfaces. *ACS Appl. Mater. Interfaces* **2018**, *10*, 10379−10387.
(33) Hanbicki, A. T.; Chuang, H. J.; Rosenberger, M. R.; Hellberg, C. S.; Sivaram, S. V.; McCreary, K. M.; Mazin, I. I.; Jonker, B. T. Double Indirect Interlayer Exciton in a MoSe2/WSe2 van der Waals Heterostructure. *ACS Nano* **2018**, *5*, 4719−4726.
(34) Schwartz, J. J.; Chuang, H. J.; Rosenberger, M. R.; Sivaram, S. V.; McCreary, K. M.; Jonker, B. T.; Centrone, A. Chemical Identification of Interlayer Contaminants within van der Waals Heterostructures. *ACS Appl. Mater. Interfaces* **2019**, *11*, 25578−25585.
(35) Seyler, K. L.; Rivera, P.; Yu, H.; Wilson, N. P.; Ray, E. L.; Mandrus, D. G.; Yan, J.; Yao, W.; Xu, X. Signatures of Moiré-Trapped Valley Excitons in $MoSe_2/WSe_2$ Heterobilayers. *Nature* **2019**, *567*, 66−70.
(36) Tran, K.; Moody, G.; Wu, F.; Lu, X.; Choi, J.; Kim, K.; Rai, A.; Sanchez, D. A.; Quan, J.; Singh, A.; Embley, J.; Zepeda, A.; Campbell, M.; Autry, T.; Taniguchi, T.; Watanabe, K.; Lu, N.; Banerjee, S.; Silverman, K.; Kim, S.; Tutuc, E.; Yang, L.; MaDonald, A. H.; Li, X. Evidence for Moiré Excitons in van der Waals Heterostructures. *Nature* **2019**, *567*, 71−75.
(37) Cheng, J.; Huang, D.; Jiang, T.; Shan, Y.; Li, Y.; Wu, S.; Liu, W. T. Chiral Selection Rules for Multi-Photon Processes in Two-Dimensional Honeycomb Materials. *Opt. Lett.* **2019**, *44*, 2141−2144.
(38) Cao, T.; Wang, G.; Han, W.; Ye, H.; Zhu, C.; Shi, J.; Niu, Q.; Tan, P.; Wang, E.; Liu, B.; Feng, J. Valley-Selective Circular Dichroism of Monolayer Molybdenum Disulphide. *Nat. Commun.* **2012**, *3*, 887.
(39) Xiao, D.; Liu, G. B.; Feng, W.; Xu, X.; Yao, W. Coupled Spin and Valley Physics in Monolayers of MoS 2 and Other Group-VI Dichalcogenides. *Phys. Rev. Lett.* **2012**, *108*, 196802.
(40) Xiao, J.; Ye, Z.; Wang, Y.; Zhu, H.; Wang, Y.; Zhang, X. Nonlinear Optical Selection Rule Based on Valley-Exciton Locking in Monolayer WS_2. *Light: Sci. Appl.* **2015**, *4*, 366.
(41) Hagimoto, K.; Mito, A. Determination of the Second-Order Susceptibility of Ammonium Dihydrogen Phosphate and α-Quartz at 633 and 1064 nm. *Appl. Opt.* **1995**, *34*, 8276−8282.
(42) Edelberg, D.; Rhodes, D.; Kerelsky, A.; Kim, B.; Wang, J.; Zangiabadi, A.; Kim, C.; Antony, A.; Ardelean, J.; Scully, M.; Scullion, D.; Embon, L.; Zu, R.; Santos, E.; Balicas, L.; Marianetti, C.; Barmak, K.; Zhu, X.; Hone, J.; Pasupathy, A. Approaching the Intrinsic Limit in Transition Metal Diselenides *via* Point Defect Control. *Nano Lett.* **2019**, *19*, 4371−4379.
(43) Wang, L.; Meric, I.; Huang, P. Y.; Gao, Q.; Gao, Y.; Tran, H.; Taniguchi, T.; Watanabe, K.; Campos, L. M.; Muller, D. A.; Guo, J.; Kim, P.; Hone, J.; Shepard, K. L.; Dean, C. R. One-Dimensional Electrical Contact to a Two-Dimensional Material. *Science* **2013**, *342*, 614−617.

https://dx.doi.org/10.1021/acsnano.9b07555
ACS Nano XXXX, XXX, XXX−XXX